

Kinetically controlled Z-alkene synthesis using iron-catalysed allene dialkylation

In the format provided by the authors and unedited

Table of contents

1. General.....	2
Solvents.....	2
Allene substrates	2
Alkyl halide substrates	16
Dialkylzinc reagents.....	16
2. Supplementary table.....	17
Supplementary table S1	17
Supplementary table S2	17
Supplementary table S3	18
3. Fe-catalyzed allene dialkylation	19
Experimental procedures	19
Synthesis of biologically active compound	43
Substrate scope limitations	44
4. Mechanistic investigations.....	45
Radical clock experiment.....	45
Detection of radical homocoupling by-products of prenyl bromide.....	46
Radical inhibitor experiment.....	46
Exclusion of halogen-atom transfer (XAT) pathways	47
Possible catalytic cycle	48
5. Density functional theory (DFT) calculations	49
5.1 Computational methods	49
5.2 Model reaction	50
5.3 Addition of ethyl radical to allene	50
5.4 Reductive elimination	58
5.5 Thermodynamics of the products.....	59
5.6 Product selectivity studies using ligand L1	60
5.7 Optimized structures and absolute energies.....	61
6. NMR spectra	64
7. References.....	119

standard and a small aliquot of the organic phase was removed for GC, GCMS and HRMS (EI) analysis.

Possible catalytic cycle

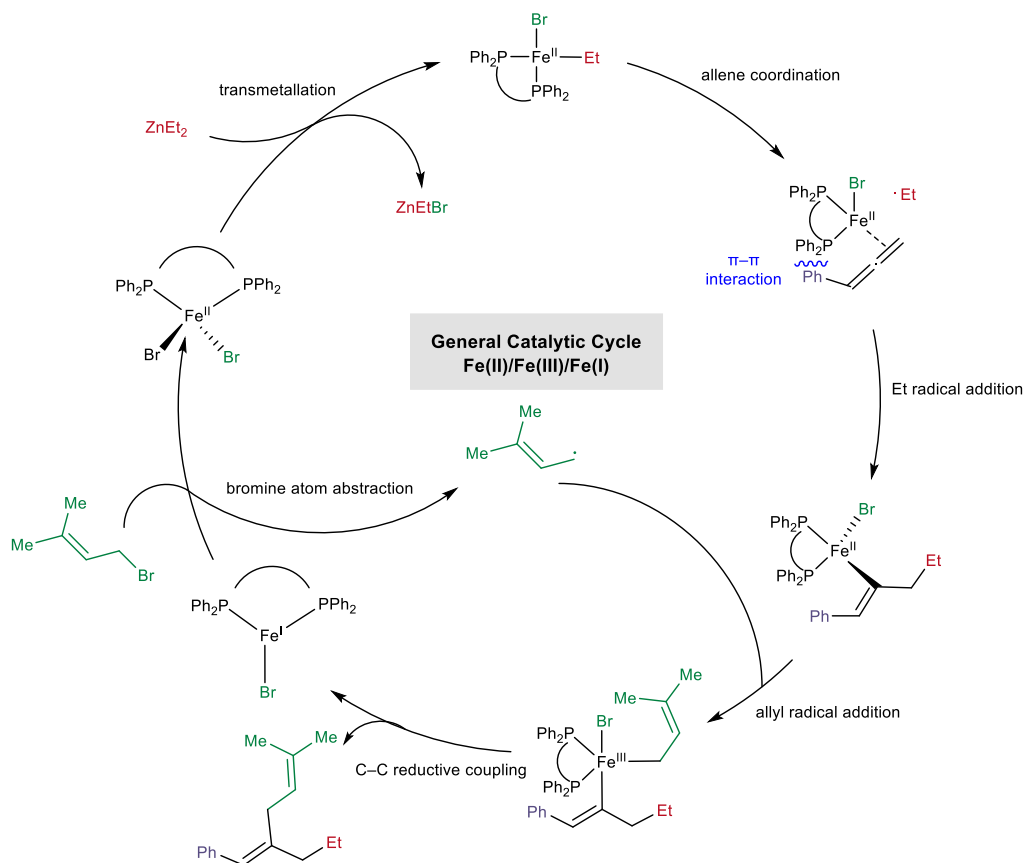


Fig. S3. Proposed mechanism for Fe-catalyzed allene dialkylation.

5. Density functional theory (DFT) calculations

5.1 Computational methods

Kohn-Sham density functional theory (KS-DFT) calculations were performed with *Gaussian 16* rev. B.01¹⁴. Geometry optimizations were performed using the B3LYP hybrid functional¹⁵⁻¹⁸ with Grimme's D3 dispersion correction with Becke-Johnson damping¹⁹ (hereafter denoted B3LYP-D3BJ) and the def2-SVP²⁰ Karlsruhe-family basis set for all atoms. Minima and transition structures on the potential energy surface (PES) were confirmed using harmonic frequency analysis at the same level of theory, showing respectively zero and one imaginary frequency. Where appropriate, intrinsic reaction coordinate (IRC) analysis were carried out to connect the appropriate reactant/product states passing through a given transition state.

Single point (SP) corrections were performed using B3LYP-D3BJ and def2-TZVP²⁰ basis set for all atoms. The SMD implicit continuum solvation model²¹ was used to account for the effect of tetrahydrofuran (THF) solvent on the computed Gibbs energy profile. Gibbs energies were evaluated at the reaction temperature of 60 °C, using Grimme's scheme of quasi-RRHO treatment of vibrational entropies²², using the GoodVibes code²³. Vibrational entropies of frequencies below 100 cm⁻¹ were obtained according to a free rotor description, using a smooth damping function to interpolate between the two limiting descriptions. The free energies reported in Gaussian from gas-phase optimisation were further corrected using standard concentration of 1 mol/L²⁴⁻²⁶, which were used in solvation calculations, instead of the gas-phase 1 atm used by default in Gaussian program.

Unless otherwise stated, the final SMD (THF)-B3LYP-D3BJ/def2-TZVP//B3LYP-D3BJ/def2-SVP Gibbs energies are used for discussion throughout. *All Gibbs energy values in the text and figures are quoted in kcal mol⁻¹.*

For species involving open-shell characteristics, including doublet, triplet, quartet, quintet and sextet radicals, we performed above-mentioned DFT methodologies using the unrestricted formalism of the Kohn-Sham theory (UKS-DFT). The eigenvalues of the spin operator S^2 after annihilation of spin contamination were checked to ensure

that they comply with the expected value of $S(S+1) = 0.75$ for a doublet wavefunction and $S(S+1) = 2$ for triplet, $S(S+1) = 3.75$ for quartet, $S(S+1) = 6$ for quintet, $S(S+1) = 8.75$ for sextet, indicating that spin contamination is not a problem for the present methodology.

All molecular structures and spin density plots were visualized using *PyMOL*²⁷ software.

5.2 Model reaction

Figure S4 shows the model reaction that we used for computational studies of reaction mechanism for the present Fe-catalysed allene dialkylation.

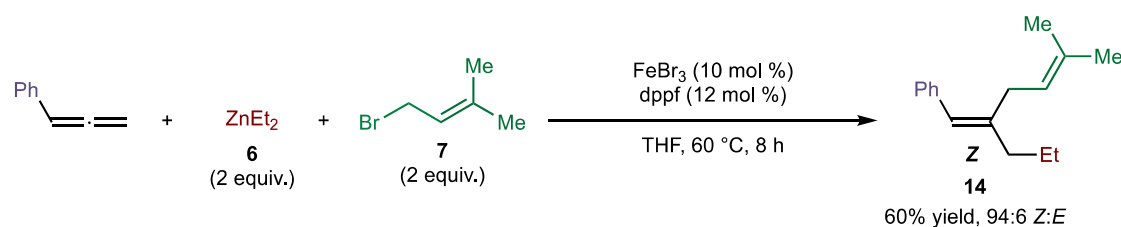


Fig. S4. Model reaction used in computational modelling.

5.3 Addition of ethyl radical to allene

5.3.1 Outer-sphere mechanism

Conformations of the competing transition state (TS) structures of the rate-determining step (addition of ethyl radical to allene) in the quintet state have been sampled and the different TS conformers are shown in Figure S5. We then took the lowest energy conformers for each competing pathway (**TS1** and **TS1'**) and optimise the TS structure for the triplet state (**TS1_triplet** and **TS1'_triplet**) and the openshell singlet state (**TS1_singlet_os** and **TS1'_singlet_os**) and found that the quintet state has the most favourable energy barrier for the addition of ethyl radical to Fe-coordinated allene substrate.

For the pathway resulting in the *Z*-product (major pathway), **TS1**, in quintet state, has a barrier of 27.4 kcal/mol whereas the triplet state (**TS1_triplet**) has a barrier of 30.7 kcal/mol and the openshell singlet state (**TS1_singlet_os**) has a much higher barrier of 49.0 kcal/mol. For the pathway leading to the *E*-product (minor pathway), **TS1'**, in

quintet state, has a barrier of 30.8 kcal/mol whereas the triplet state (**TS1_triplet**) has a barrier of 48.6 kcal/mol and the openshell singlet state (**TS1_singlet_os**) has a much higher barrier of 54.1 kcal/mol.

The barrier difference $\Delta\Delta G^\ddagger$ between **TS1** and **TS1'** gives a kinetic preference for the major product by a factor of 170 : 1, using simple transition state theory as an estimate and without Boltzmann weighting of all the conformers via the following:

The Eyring equation

$$k = \frac{k_B T}{h} e^{-\Delta G^\ddagger / RT}$$

gives the rate constant under simple transition state theory (TST) assumptions.

Under kinetic control, as we compare the barrier heights difference between competing transition states, the ratio of the rates between two pathways is given by:

$$\frac{k_A}{k_B} = \frac{e^{-\Delta G_A^\ddagger / RT}}{e^{-\Delta G_B^\ddagger / RT}} = e^{-\Delta\Delta G^\ddagger / RT}$$

where k_X is the rate constant of pathway X (X=A or B); ΔG_X^\ddagger is the activation barrier for pathway X; and $\Delta\Delta G_X^\ddagger$ is the difference in the barrier heights; and R is the gas constant, T the temperature. Note that the Eyring Equation pre-exponential factor cancels when comparing the ratio of the rate constants. Thus, using the calculated $\Delta\Delta G_X^\ddagger$ value (difference of barrier heights between competing TSs) at the reaction temperature (e.g., 60 °C = 313.15K), we are able to obtain the ratio of competing rates.

TS1	TS1'
$\Delta G^\ddagger = 27.4$	$\Delta G^\ddagger = 30.8$

<p style="text-align: center;">TS1-c2</p>	<p style="text-align: center;">TS1'-c2</p>
<p style="text-align: center;">$\Delta G^\ddagger = 32.5$</p>	<p style="text-align: center;">$\Delta G^\ddagger = 32.3$</p>
<p style="text-align: center;">TS1-c3</p>	<p style="text-align: center;">TS1'-c3</p>
<p style="text-align: center;">$\Delta G^\ddagger = 34.5$</p>	<p style="text-align: center;">$\Delta G^\ddagger = 32.8$</p>

TS1-c4	TS1'-c4
$\Delta G^\ddagger = 35.8$	$\Delta G^\ddagger = 38.0$
TS1_triplet	TS1'_triplet
$\Delta G^\ddagger = 30.7$	$\Delta G^\ddagger = 48.6$

TS1_singlet_os	TS1'_singlet_os
$\Delta G^\ddagger = 49.0$	$\Delta G^\ddagger = 54.1$
TS2_quartet	TS2_sextet
$\Delta G^\ddagger = -6.9$	$\Delta G^\ddagger = -0.7$

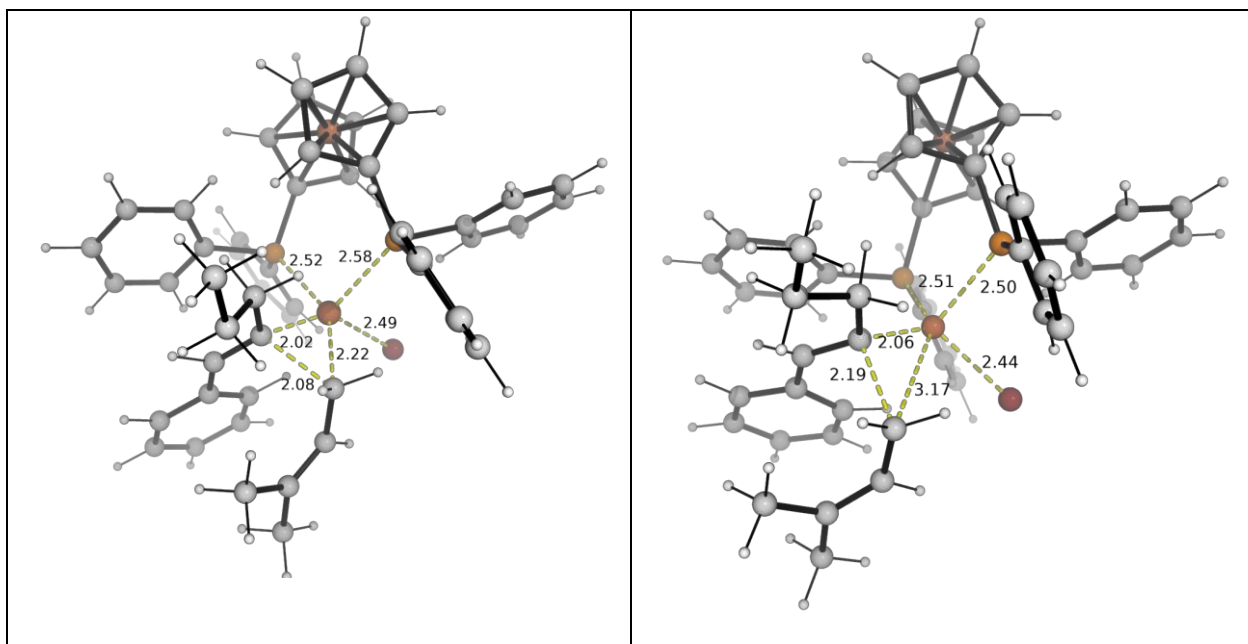


Fig. S5. DFT-optimized TS structures for the addition of ethyl radical to allene substrate coordinated to Fe centre. All TSs are in quintet state if not specified; triplet = triplet state; singlet_os = openshell singlet. Gibbs energies are taken relative to the most stable complex **I** and the values are given in kcal/mol.

	TS1	TS1'
$\Delta\Delta G^\ddagger$	0.0 kcal/mol	3.4 kcal/mol
DFT structure		

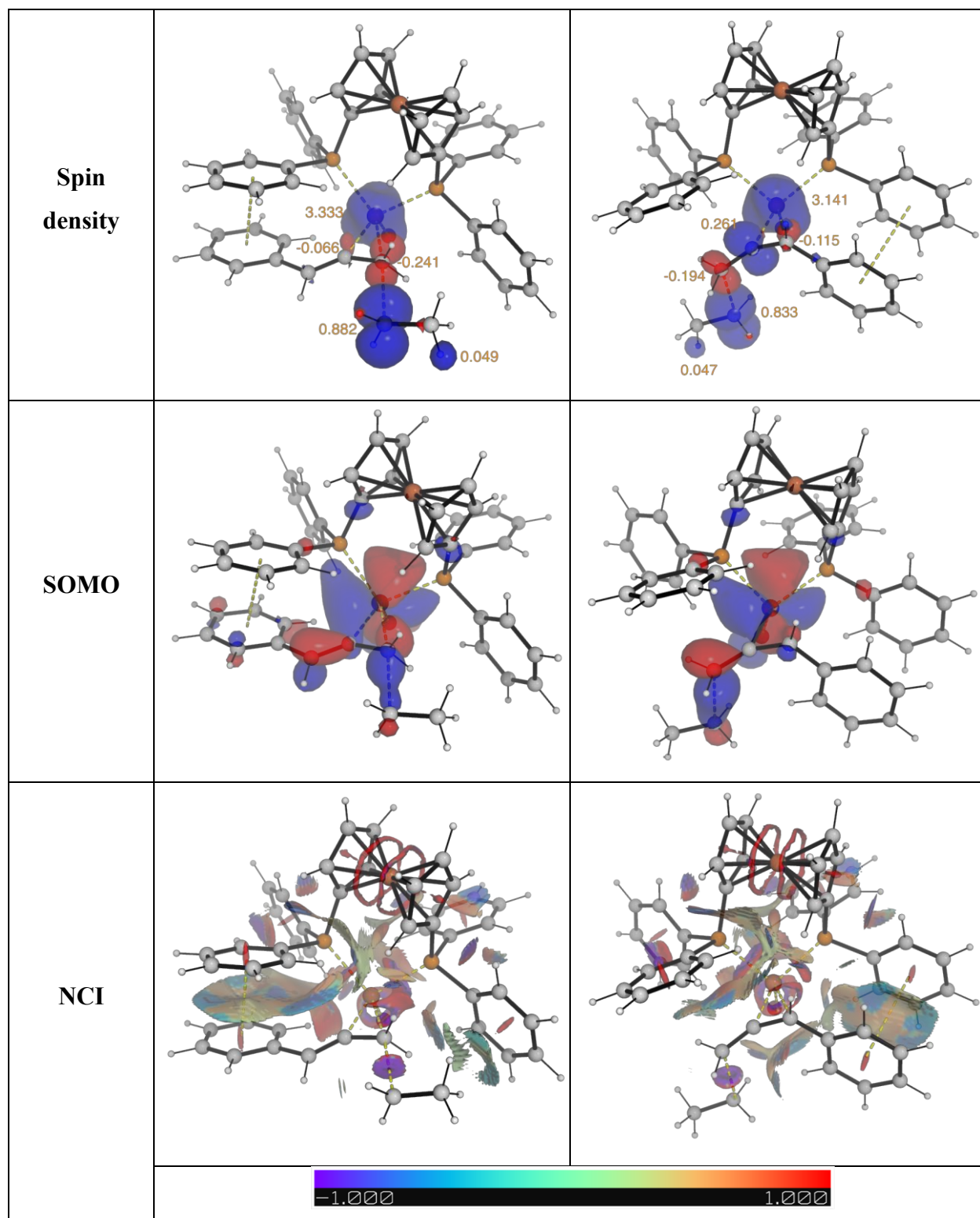
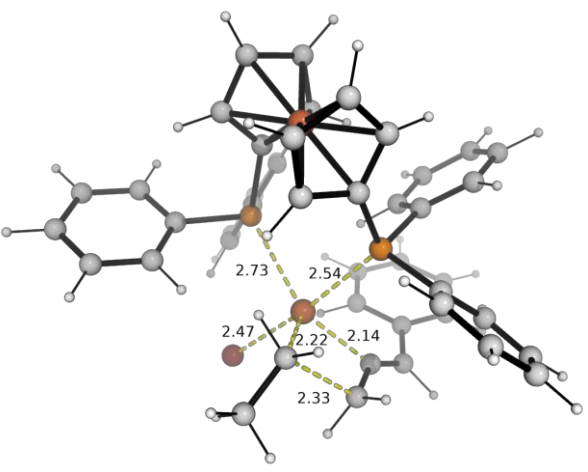
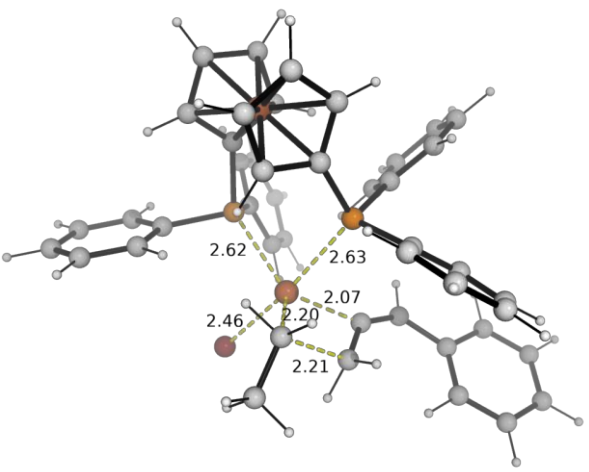


Fig. S6. Detailed analysis of the competing transition states for the rate-determining step. Spin density, singly occupied molecular orbitals (SOMO) and non-covalent interaction (NCI) plots are shown. Spin density plots were visualized at an isosurface value of 0.005 a.u., SOMOs are visualized at 0.025 a.u., and the NCI plots were visualized at an isosurface value for the gradient at 0.5 a.u..

5.3.2 Inner-sphere mechanism

The inner-sphere mechanism wherein the ethyl radical first coordinates to the Fe-centre to give Fe(II) species before addition to allene has a much higher barrier. The DFT optimised structures and the activation barrier heights are shown in Figure S7.

For this mechanistic pathway, the TS leading to the minor product (**TS1a'**) has a lower barrier than the TS leading to the major product (**TS1a**), which would predict the opposite selectivity as observed experimentally. In addition, these barriers are much higher than the TSs via outer-sphere mechanism (**TS1** and **TS1'**), by at least 12.6 kcal/mol, discussed previously. Thus the inner-sphere mechanism is much less favoured than the outer-sphere mechanism.

TS1a	TS1a'
$\Delta G^\ddagger = 41.3$	$\Delta G^\ddagger = 40.0$
	
TS1a-c2	TS1a'-c2
$\Delta G^\ddagger = 46.5$	$\Delta G^\ddagger = 40.8$

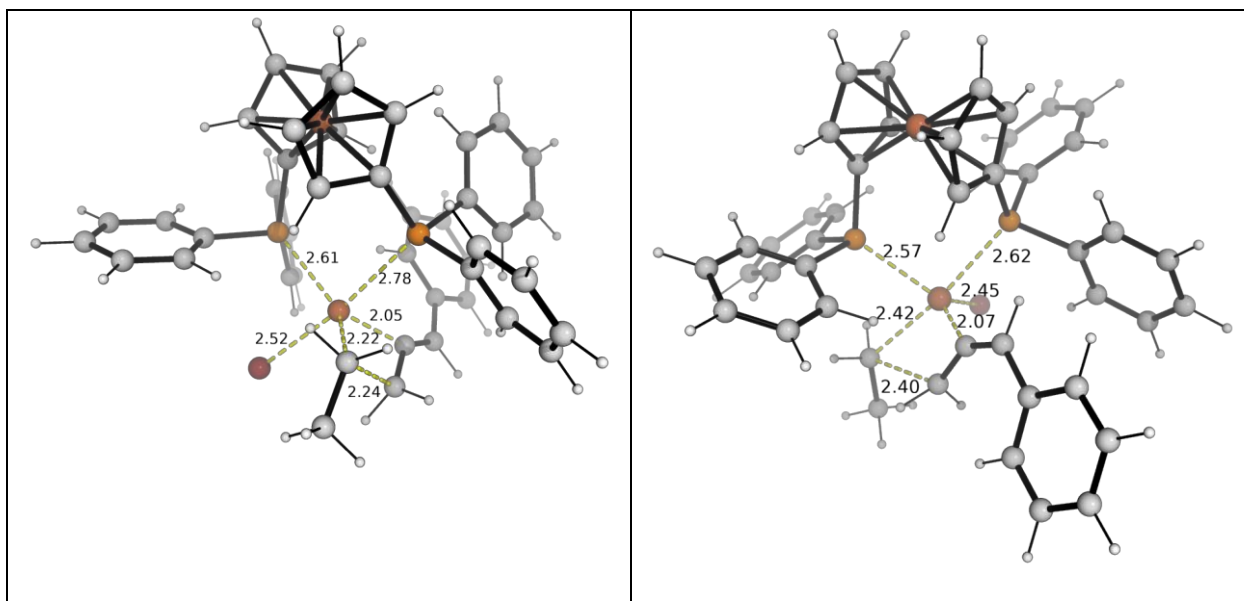


Fig. S7. DFT-optimized TS structures for the addition of ethyl radical to allene substrate coordinated to Fe centre via inner-sphere mechanism. All TSs are in quintet state. Gibbs energies are taken relative to the most stable complex **I** and the values are given in kcal/mol.

5.4 Reductive elimination

The reductive coupling of allyl radical and the alkyliron intermediate via **TS2** has lower barrier than **TS1** and is thus not the rate-determining step. In the quartet state, the allylic radical coordinates to the Fe-centre and carries out an inner-sphere reductive C–C bond formation (**TS2_{quartet}**, Figure S8) as evidenced by the short Fe–C(allyl) bond distance (2.22 Å). IRC analysis indicates that the species before this TS has the allyl group coordinated to the Fe-centre. On the other hand, in the sextet state, the allylic radical does not coordinate to the Fe-centre and carries out an outer-sphere reductive C–C bond formation (**TS2_{sextet}**, Figure S8) as evidenced by the much longer Fe–C(allyl) bond distance (3.17 Å). IRC analysis indicates that the species before this TS has the allyl group not coordinated to the Fe-centre.

TS2_{quartet}	TS2_{sextet}
$\Delta G^\ddagger = -6.9$	$\Delta G^\ddagger = -0.7$

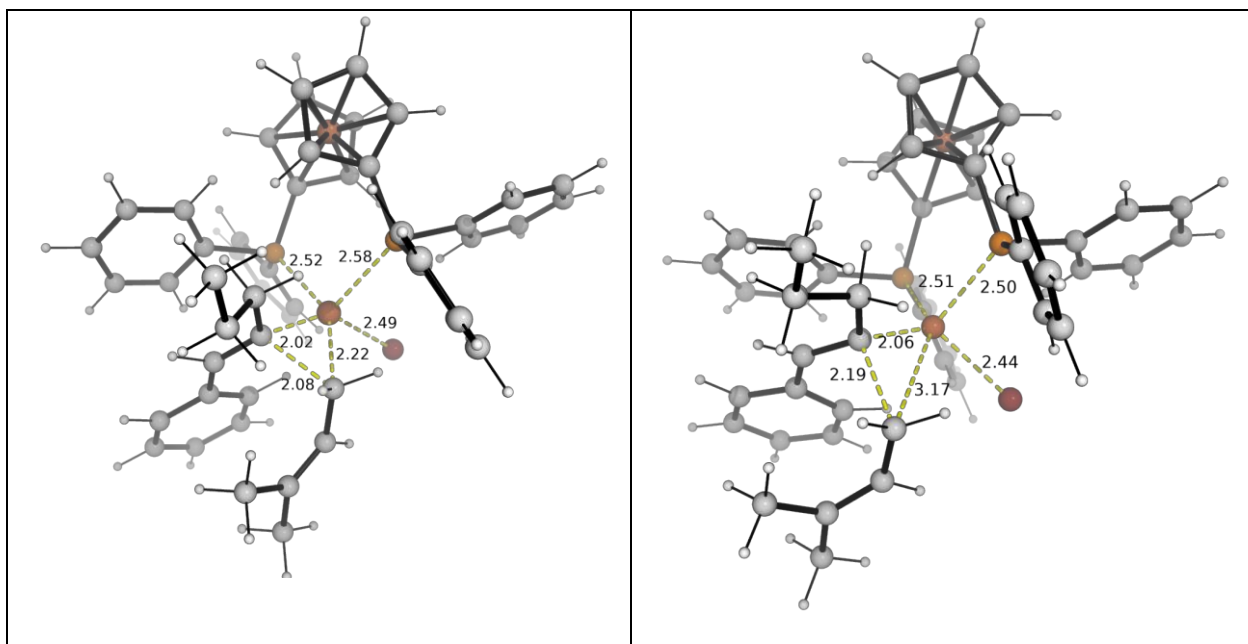


Fig. S8. DFT-optimized TS structures for the reductive C–C coupling of allyl radical and alkenyliron intermediate. All TSs are in quintet state. Gibbs energies are taken relative to the most stable complex **I** and the values are given in kcal/mol.

5.5 Thermodynamics of the products

The thermodynamic stability of the *E* vs *Z* isomers was compared (Figure S9). These two isomers are almost energetic with the *E* isomer being slightly more stable than the *Z* isomer, by 0.2 kcal/mol.

E_product	Z_product
$\Delta\Delta G = 0.0$	$\Delta\Delta G = 0.2$

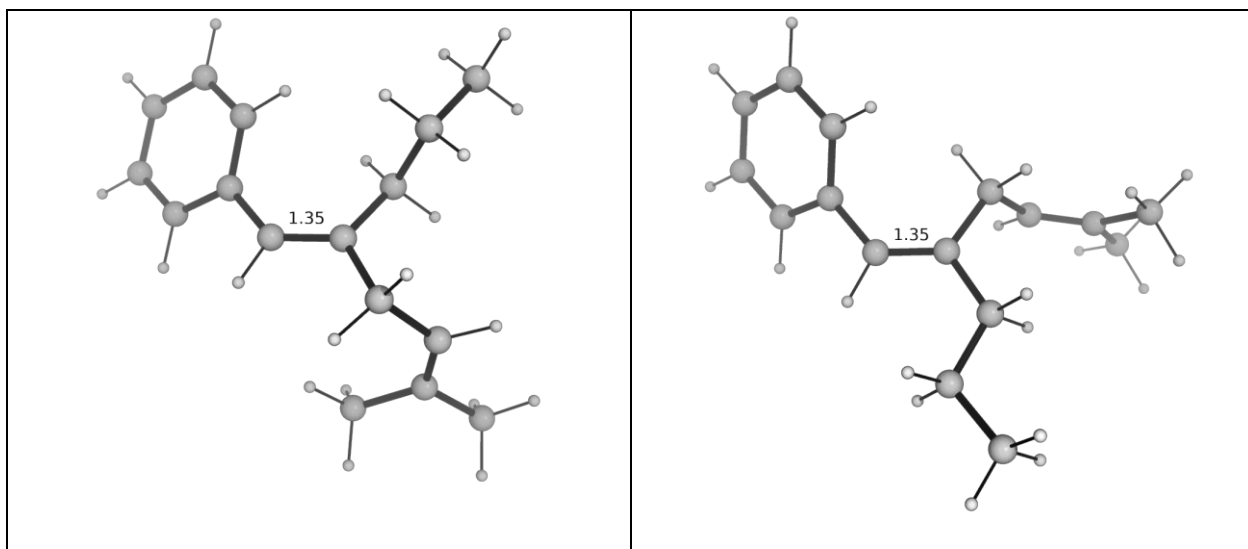


Fig. S9. DFT-optimized product structures. Gibbs energies are taken relative to the most stable product and the values are given in kcal/mol.

5.6 Product selectivity studies using ligand L1

To understand the effect of ligands on the product selectivity, we performed computational studies on the rate-determining transition state (first C–C coupling step) of the competing pathways using ligand **L1**. We successfully located the TSs and the DFT-optimized structures are shown in Figure S10, with their relative activation barriers. We see that the major pathway leading eventually to the *Z* product via **TS1_L1**, has a lower barrier, by 0.4 kcal/mol, than the minor pathway leading eventually to the *E* product via **TS1'_L1**. This would translate to a ratio of *Z*:*E* of 1.8:1, using simple transition state theory. As this small difference between the barrier heights (<0.5 kcal/mol) easily falls within the error of the theoretical methods, we expect that the product will be a mixture of *Z* and *E* olefins.

This is perhaps an implication of the ligand, as can be seen from the DFT-optimized structures in Figure S10, that the allene substrate will interact with the π -system of ligand **L1**, via either face. After the allene binds, there is no steric differences for the ethyl radical to favor attack of the terminal carbon of allene from one side over the other, due to the open nature of the terminal carbon for attack from either side. Thus, poor stereoselectivity is expected using planar ligands such as ligand **L1**.

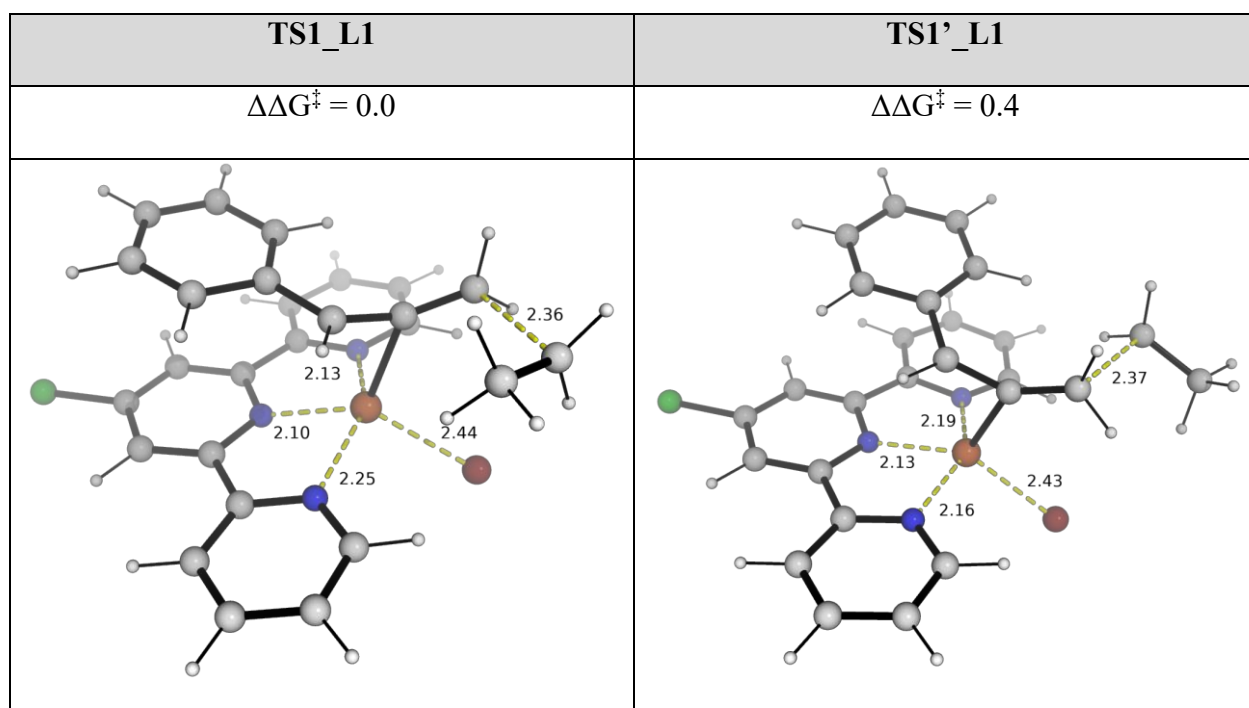


Fig. S10. DFT-optimized transition state structures of the rate-determining step of first C–C bond formation, using ligand **L1**. Gibbs energies are taken relative to the most stable TS and the values are given in kcal/mol.

5.7 Optimized structures and absolute energies

Geometries of all optimized structures (in *.xyz* format with their associated gas-phase energy in Hartrees) are included in a separate folder named *DFT_optimised_xyz_structures* with an associated *readme.txt* file. All these data have been uploaded to <https://zenodo.org/records/11363682> (DOI: 10.5281/zenodo.11363682).

Absolute values (in Hartrees) for SCF energy, zero-point vibrational energy (ZPE), enthalpy and quasi-harmonic Gibbs free energy (at 60 °C/333.15 K) for optimized structures are given below. Single point corrections in SMD THF using B3LYP-D3BJ/def2-TZVP level of theory are also included.

Structure	E/au	ZPE/au	H/au	T.S/au	qh-G/au	SP SMD(THF)- B3LYP- D3BJ/def2- TZVP
-----------	------	--------	------	--------	---------	---

phenylallene	-347.500243	0.137391	-347.35234	0.044579	-347.396289	-347.887587
ethyl_radical	-79.105489	0.058818	-79.040995	0.029806	-79.070703	-79.19780953
allyl_radical	-195.77536	0.121625	-195.64546	0.038418	-195.683863	-195.9975524
I_singlet	-7174.577766	0.586472	-7173.9438	0.128017	-7174.062065	-7176.994847
I_triplet	-7174.595684	0.58445	-7173.9629	0.132643	-7174.08455	-7177.013908
I_quintet	-7174.610012	0.583483	-7173.9771	0.13751	-7174.102154	-7177.028444
II_quintet	-7522.13079	0.722664	-7521.3472	0.163497	-7521.494657	-7524.926993
III_quintet	-7522.109212	0.720064	-7521.3278	0.162641	-7521.475355	-7524.903296
TS1	-7522.10083	0.72044	-7521.3202	0.159294	-7521.465142	-7524.896317
TS1_c2	-7522.094575	0.720304	-7521.3139	0.159754	-7521.459154	-7524.887877
TS1_c3	-7522.091256	0.720546	-7521.3103	0.16102	-7521.456071	-7524.884433
TS1_c4	-7522.086476	0.717985	-7521.3073	0.162535	-7521.454647	-7524.879068
TS1'	-7522.097457	0.720931	-7521.3165	0.160065	-7521.461608	-7524.891063
TS1'_c2	-7522.099297	0.721805	-7521.3178	0.157533	-7521.461453	-7524.890644
TS1'_c3	-7522.096416	0.722075	-7521.3148	0.156537	-7521.45807	-7524.890338
TS1'_c4	-7522.090663	0.721943	-7521.309	0.158286	-7521.453126	-7524.881245
TS1_triplet	-7522.097215	0.721249	-7521.3161	0.157363	-7521.459605	-7524.892854
TS1_singlet_os	-7522.069011	0.720923	-7521.2881	0.157229	-7521.430947	-7524.864135
TS1'_triplet	-7522.072623	0.721713	-7521.2913	0.158082	-7521.434883	-7524.864476
TS1'_singlet_os	-7522.066103	0.722285	-7521.2845	0.153959	-7521.425556	-7524.85861
TS1a	-7522.08795	0.722878	-7521.306	0.154742	-7521.448086	-7524.878251
TS1a_c2	-7522.077468	0.723898	-7521.2948	0.155365	-7521.436789	-7524.870831
TS1a'	-7522.084672	0.72312	-7521.3023	0.159803	-7521.446406	-7524.878686
TS1a'_c2	-7522.084798	0.723322	-7521.3022	0.158945	-7521.446066	-7524.877948
IV_quintet	-7522.192235	0.72821	-7521.4052	0.156182	-7521.547494	-7524.982215
IV'_quintet	-7522.182824	0.728317	-7521.3953	0.160554	-7521.539251	-7524.977082
V_sextet	-7717.986051	0.851508	-7717.0655	0.179872	-7717.227867	-7720.990534
V_doublet	-7717.947591	0.853489	-7717.0263	0.172924	-7717.184173	-7720.951084
V_quartet	-7717.986322	0.851656	-7717.0657	0.179084	-7717.227461	-7720.990561
VI_quartet	-7717.992824	0.855264	-7717.0701	0.172997	-7717.228231	-7720.993809
TS2_quartet	-7717.984077	0.854885	-7717.0624	0.172046	-7717.219325	-7720.986052
VII_quartet	-7718.044443	0.857594	-7717.1199	0.172246	-7717.277003	-7721.043758
TS2_sextet	-7717.970167	0.852275	-7717.0505	0.173858	-7717.2089	-7720.972632
VII_sextet	-7717.994939	0.855024	-7717.0724	0.17527	-7717.231306	-7720.996215
Z_product	-622.5558	0.335339	-622.19806	0.075052	-622.268235	-623.2452905
E_product	-622.557144	0.335672	-622.19922	0.073898	-622.268584	-623.246613

TS1_L1	-5465.728795	0.420246	-5465.2699	0.112702	-5465.37457	-5467.657208
TS1'_L1	-5465.726818	0.420797	-5465.2676	0.111238	-5465.371554	-5467.657657

7. References

1. Kuang, J. & Ma, S. An efficient synthesis of terminal allenes from terminal 1-alkynes. *J. Org. Chem.* **74**, 1763–1765 (2009).
2. Yonehara, M., Nakamura, S., Muranaka, A. & Uchiyama, M. Regioselective silylzincation of phenylallene derivatives. *Chem. Asian J.* **5**, 452–455 (2010).
3. Nakamura, H., Kamakura, T., Ishikura, M. & Biellmann, J.-F. Synthesis of allenes via palladium-catalyzed hydrogen-transfer reactions: propargylic amines as an allenyl anion equivalent. *J. Am. Chem. Soc.* **126**, 5958–5959 (2004).
4. Rochat, R. *et al.* Organomagnesium-catalyzed isomerization of terminal alkynes to allenes and internal alkynes. *Chem. Eur. J.* **21**, 8112–8120 (2015).
5. Matsubara, T., Takahashi, K., Ishihara, J. & Hatakeyama, S. Total synthesis of (-)-ophiodilactone A and (-)-ophiodilactone B. *Angew. Chem. Int. Ed.* **53**, 757–760 (2014).
6. Liu, J., Han, Z., Wang, X., Wang, Z. & Ding, K. Highly regio- and enantioselective alkoxycarbonylative amination of terminal allenes catalyzed by a spiroketal-based diphosphine/Pd(II) complex. *J. Am. Chem. Soc.* **137**, 15346–15349 (2015).
7. Puriņš, M., Eichenbergera, L. & Waser, J. Synthesis of propargyl silanes from terminal alkynes via a migratory Sonogashira reaction. *Chem. Commun.* **59**, 7931–7934 (2023).
8. Nakamura, H., Onagi, S. & Kamakura, T. Synthesis of heterocyclic allenes via palladium-catalyzed hydride-transfer reaction of propargylic amines. *J. Org. Chem.* **70**, 2357–2360 (2005).
9. Detistova, G. I. *et al.* Photoredox-catalyzed hydrosulfonylation of arylallenes. *J. Org. Chem.* **85**, 2250–2259 (2020).
10. Zhao, Z., Racicot, L. & Murphy, G. K. Fluorinative rearrangements of substituted phenylallenes mediated by (difluoroiodo)toluene: synthesis of α -(difluoromethyl)styrenes. *Angew. Chem. Int. Ed.* **56**, 11620–11623 (2017).

11. Hayashi, S., Hirano, K., Yorimitsu, H. & Oshima, K. Synthesis of arylallenes by palladium-catalyzed retro-propargylation of homopropargyl alcohols. *J. Am. Chem. Soc.* **130**, 5048–5049 (2008).
12. Krasovskiy, A. & Knochel, P. Convenient titration method for organometallic zinc, magnesium, and lanthanide reagents. *Synthesis* **5**, 890–891 (2006).
13. Childers, W. *et al.* Novel compounds that reverse the disease phenotype in Type 2 Gaucher disease patient-derived cells. *Bioorg. Med. Chem. Lett.* **30**, 126806 (2020).
14. Frisch, M. J. *et al.* *Gaussian, Inc., Wallingford CT, Gaussian 16, Revision B.01.* (2016).
15. Becke, A. D. Density-functional thermochemistry. III. The role of exact exchange. *J. Chem. Phys.* **98**, 5648–5652 (1993).
16. Lee, C., Yang, W. & Parr, R. G. Development of the colle-salvetti correlation-energy formula into a functional of the electron density. *Phys. Rev. B* **37**, 785–789 (1988).
17. Vosko, S. H., Wilk, L. & Nusair, M. Accurate spin-dependent electron liquid correlation energies for local spin density calculations: A critical analysis. *Can. J. Phys.* **58**, 1200–1211 (1980).
18. Stephens, P. J., Devlin, F. J., Chabalowski, C. F. & Frisch, M. J. Ab initio calculation of vibrational absorption and circular dichroism spectra using density functional force fields. *J. Phys. Chem.* **98**, 11623–11627 (1994).
19. Grimme, S., Antony, J., Ehrlich, S. & Krieg, H. A consistent and accurate Ab initio parametrization of density functional dispersion correction (DFT-D) for the 94 elements H-Pu. *J. Chem. Phys.* **132**, 154104 (2010).
20. Weigend, F. & Ahlrichs, R. Balanced basis sets of split valence, triple zeta valence and quadruple zeta valence quality for H to Rn: design and assessment of accuracy. *Phys. Chem. Chem. Phys.* **7**, 3297–3305 (2005).
21. Marenich, A. V., Cramer, C. J. & Truhlar, D. G. Universal solvation model based on solute electron density and on a continuum model of the solvent defined by the bulk dielectric constant and atomic surface tensions. *J. Phys. Chem. B* **113**, 6378–6396 (2009).

22. Grimme, S. Supramolecular binding thermodynamics by dispersion-corrected density functional theory. *Chem.: Eur. J.* **18**, 9955–9964 (2012).
23. Luchini, G. *et al.* GoodVibes: Automated thermochemistry for heterogeneous computational chemistry data. *F1000Research*, **9**, 291 (2020).
24. Bryantsev, V. S., Diallo, M. S., Goddard Iii, W. A. & Goddard, W. A. Calculation of solvation free energies of charged solutes using mixed cluster/continuum models. *J. Phys. Chem. B* **112**, 9709–9719 (2008).
25. Boyle, B. T., Levy, J. N., de Lescure, L., Paton, R. S. & McNally, A. Halogenation of the 3-position of pyridines through zinc imine intermediates. *Science* **378**, 773–779 (2022).
26. Darù, A., Hu, X. & Harvey, J. N. Iron-catalyzed reductive coupling of alkyl iodides with alkynes to yield cis-olefins: Mechanistic insights from computation. *ACS Omega* **5**, 1586–1594 (2020).
27. Schrödinger, L. *The PyMOL molecular graphics development component*, Version 1.8 (2015).